

# A high order differential equation based wall distance solver

Hemanth Chandra Vamsi Kakumani<sup>a,\*</sup>, Nagabhushana Rao Vadlamani<sup>b</sup>

<sup>a,b</sup>*Department of Aerospace Engineering, Indian Institute of Technology Madras, Chennai, 600036, India*

<sup>\*</sup>*Present address: Technion Israel Institute of Technology, Haifa, 3200003, Israel, hemanth@campus.technion.ac.il*

---

## Abstract

A computationally efficient high-order solver is developed to compute the wall distances, which are typically used for turbulence modelling, peripheral flow simulations, Computer Aided Design (CAD) etc. The wall distances are computed by solving the differential equations namely: Eikonal, Hamilton-Jacobi (H-J) and Poisson. The computational benefit of using high-order schemes (explicit/compact schemes) for wall-distance solvers, both in terms of accuracy and computational time, has been demonstrated. A new H-J formulation based on the localized artificial diffusivity (LAD) approach has been proposed, which has produced results with an accuracy comparable to that of the Eikonal formulation. When compared to the baseline H-J solver using upwind schemes, the solution accuracy has improved by an order of magnitude and the calculations are  $\approx 5$  times faster using the modified H-J formulation. A modified curvature correction has also been implemented into the H-J solver to account for the near-wall errors due to concave/convex wall curvatures. The performance of the solver using different schemes has been tested both on the steady canonical test cases and the unsteady test cases like ‘piston-cylinder arrangement’, ‘bouncing cube’ and ‘burning of a star grain propellant’ where the wall-distance evolves with time.

*Keywords:* Wall distance, High order schemes, Hamilton-Jacobi equation, Localized Artificial Diffusivity (LAD).

---

## 1. Introduction

Distance to the solid no-slip wall, referred to as wall-distance in the literature, is often used in the formulation of several eddy-resolving or turbulence modelling strategies. For example, original formulation of the Detached Eddy Simulations (DES) uses wall distance to switch between the modelled and resolved regions of turbulence. Reynolds Averaged Navier Stokes (RANS) [12] models like Spalart Allmaras,  $k - \epsilon$ ,  $k - \omega$  use wall-distance for the near-wall treatment. Such strategies can also be used to alter the dissipation term in the turbulence models or to introduce surface roughness effects by locally altering the length scales of flow using wall-distance [8, 10]. Wall-distances are also used in the peripheral flow applications such as multiphase flows. Accuracy of the wall-distance values and their efficient computation is important in these fluid flow simulations. In addition to Computational Fluid Dynamics (CFD), wall-distances are also encountered in other applications such as Computer Aided Design (CAD) and automated meshing.

---

\*Corresponding author

*Email address:* nrv@iitm.ac.in (Nagabhushana Rao Vadlamani<sup>b</sup>)

There are various search-based algorithms available in the literature to estimate the wall-distances [13, 14]. However, search algorithms are computationally expensive and suffer from weak scalability, specifically on large meshes and with increasing number of wall faces in the computational domain. Search algorithms also produce inaccurate solutions on non-orthogonal and unstructured grids due to Euclidian and projection based measurement approaches they employ. Search approaches can sometimes produce non-smooth or heavily discontinuous solutions, particularly on low-quality meshes which are non-orthogonal and highly skewed. These inaccuracies can lead to convergence issues of the flow simulations.

On the other hand, differential equation based wall-distance algorithms [2, 3, 4] overcome most of the limitations encountered by the search-based algorithms. These approaches are highly scalable, much more accurate than search-based algorithms and produce smoother solutions in the computational domain. Three classes of differential equation based wall-distance approach include: Eikonal, Hamilton-Jacobi (H-J) and Poisson equations, which will be described in detail in the subsequent section. The formulations of these equations is similar to those of the differential equations governing the flow. Hence, the wall-distance differential equations can be readily implemented into the CFD solvers taking advantage of the existing functions/subroutines of the code that are already written. In addition, the differential equation based approach is demonstrated to be robust even on poor quality grids by Tucker et al. [2]. Eikonal and H-J equations can be categorized as advection and advection-diffusion equations respectively. Tucker et al. [2] has proposed a first order upwinding method to drive the wall-distance equations to a steady state solution. Although the first-order upwind spatial scheme provides good accuracy, particularly for the Eikonal equation, it involves the repeated computation of wind direction during each iteration. The CPU time consumption per iteration and consequently the overall convergence time taken is very high particularly on unstructured grids. The implementation of upwind scheme is also relatively elaborate in curvilinear coordinates when compared to the standard explicit finite difference or compact schemes.

In the context of high-fidelity eddy resolving simulations like Large Eddy Simulations (LES) or Direct Numerical Simulations (DNS), high-order schemes have been gaining increasing popularity as these schemes can accurately capture the high frequencies in the transitional/turbulent flows at a substantially lower grid count than the low-order schemes. To accurately capture turbulence, non-dissipative high order explicit and compact central schemes are preferred over the dissipative up-wind schemes. The objectives of the current work are multi-fold. Firstly, we have attempted to exploit the high-order explicit and compact spatial difference schemes (up-to 6th order) to solve the differential equations governing the wall distance. We compare the accuracy and computational efficacy of these schemes with the standard upwind schemes. A modified local artificial diffusivity based Hamilton-Jacobi formulation is also introduced, which yields wall-distance estimates as accurate as the Eikonal equation with enhanced stability characteristics. To account for the loss of wall distance accuracy near the regions of high wall curvatures, we introduce a curvature correction to the H-J equation on the basis of [22]. In contrast to the fixed wall test cases typically reported in the literature, we also demonstrate the efficacy of the current formulation on unsteady moving bodies. In these test cases, the wall-distance changes with time. It is worth mentioning that, the scope of the current study is confined to accurately capturing wall distance field using differential equation approach using high-order

schemes typically in-built in the solvers using eddy-resolving approach. Exploring the effects of these strategies on the flow-field prediction is beyond the scope of the current study.

A brief outline of the paper is as follows. Three classes of differential equations governing wall distances are described in Section 2. In Section 3, the numerical methodology employed for spatial discretization, filtering and convergence for both the baseline and enhanced solvers are described. Subsequently, details of the geometry, mesh and boundary conditions used for various validation cases are discussed in section 4. In section 5, we present the results corresponding to the validation of the baseline solver. The performance of the proposed modifications are demonstrated on several steady and unsteady test cases. Finally, a brief summary and key conclusions of the current work are given in section 6.

## 2. Governing Equations

### 2.1. Eikonal equation

The exact governing equation for wall-distance ( $\phi$ ) is the Eikonal equation (Eqn.1), which is a non-linear hyperbolic partial differential equation. It's formulation originates from the fact that the magnitude of wall distance gradient at all the points in the domain equals one [9]. The equation reads as follows.

$$|\nabla\phi| = 1 \text{ or } (\nabla\phi)^2 = 1 \text{ or } \mathbf{U} \cdot \nabla\phi = 1 \quad (1)$$

$$U_x \frac{\partial\phi}{\partial x} + U_y \frac{\partial\phi}{\partial y} + U_z \frac{\partial\phi}{\partial z} = 1 \quad (2)$$

Where  $\mathbf{U}$  in the Eqn.1 is defined as  $\nabla\phi$ , the Eikonal front propagation velocity. The equation can also be rewritten in its expanded form, Eqn.2, with  $U_x$ ,  $U_y$  and  $U_z$  as the components of  $\mathbf{U}$ . Given the non-linearity of this equation, solving it using non dissipative central schemes is challenging. High-frequency Gibbs oscillations across sharp discontinuity across the Eikonal front leads to the divergence of the solution. Dissipation of some form is required to suppress these high frequency oscillations thereby enhance the stability and ensure robust convergence. Methods to solve this equation will be described in section 3.

### 2.2. Poisson equation

Spalding [21] proposed a numerically simplistic Poisson based method to compute wall distances. The governing equation is given by:

$$\nabla^2\phi' = -1 \quad (3)$$

$$\phi = \pm \sqrt{\sum_{j=1,3} \left(\frac{\partial\phi'}{\partial x_j}\right)^2} + \sqrt{\sum_{j=1,3} \left(\frac{\partial\phi'}{\partial x_j}\right)^2} + 2\phi' \quad (4)$$

It should be noted that the approach involves solving for  $\phi'$  as the variable in the Poisson equation (Eqn.3). The actual wall distance ( $\phi$ ) is subsequently computed using the auxiliary equation, Eqn.4. However, Poisson equation can only yield accurate wall distances close to the walls. Accurate wall distance away from the walls are required for certain applications like Computer Aided Design (CAD), computing minimal surfaces, automated meshing [16] etc. Nevertheless, for most of the turbulence modelling strategies, it is sufficient to have accurate wall-distances close to the walls where the viscous effects are dominant.

### 2.3. Hamilton-Jacobi (H-J) equation

The wall distance Hamilton-Jacobi (H-J) equation was first proposed by Tucker et al. [1] in 2003. The H-J equation can be interpreted as a hybrid between the Eikonal and Poisson equations. With the advection term on the LHS and a Laplacian term on the RHS, H-J equation takes the general form Eqn 5.

$$\mathbf{U} \cdot \nabla \phi = 1 + \Gamma \nabla^2 \phi \quad (5)$$

The Laplacian operator in the equation provides the required dissipation to suppresses high frequency Gibbs oscillations originating from the advection term. Although the Laplacian operator enhances stability, the accuracy of the wall-distance estimates can deteriorate depending upon the formulation used for the term  $\Gamma$ . Nevertheless, the equation offers a good alternative to the Eikonal equation due to its superior stability and robustness.

#### 2.3.1. Standard $\Gamma$ formulation

The formulation for  $\Gamma$  is generally modelled as a linear function of  $\phi$  in the literature [1, 2] as shown in Eqn.6.

$$\Gamma = \epsilon \phi \quad (6)$$

In this equation,  $\epsilon$  is an arbitrary constant typically ranging between 0.1 and 1, chosen depending on the mesh and geometry of the simulation. This formulation gives zero value for  $\Gamma$  near the walls where  $\phi \ll 0$  (essentially solving the Eikonal equation) and progressively increases the  $\Gamma$  away from the wall. The H-J equation using this formulation is referred to as ‘standard H-J equation’ in the current work. Other non-linear variations (quadratic, cubic, logarithmic etc.) can also be used instead of Eqn.6.

#### 2.3.2. The new Localized Artificial Diffusivity (LAD) based formulation for $\Gamma$

We propose an adaptive formulation for  $\Gamma$  based on the Localized Artificial Diffusivity (LAD) approach to improve accuracy. The formulation is inline with the LAD based shock capturing method proposed by Kawai and Lele [20]. At each time step, the dispersion errors originating from the non-linear terms in the governing equation must be damped. We use an adaptive value of  $\Gamma$ , shown in the Eqn7, instead of the linear variation proposed by 6. It should be noted that  $\Gamma$  is proportional to the fourth derivative of  $\phi$ , which is useful in identifying the localized regions where the dispersion error is dominant. The new formulation introduces a desired amount of dissipation to suppress

dispersion thereby reducing the overall error in the final solution. Improvement in the solution accuracy will be demonstrated in the results section in detail.

$$\Gamma = MIN \left( \epsilon_c, C \left| \sum_{l=1}^3 \left[ \sum_{m=1}^3 \left( \frac{\partial \xi_l}{\partial x_m} \right)^2 \right]^2 \frac{\partial^4 \phi}{\partial \xi_l^4} \Delta x_l^3 \right| \right) \quad (7)$$

Here,  $\xi_l$  refers to generalized coordinates  $\xi$ ,  $\eta$  and  $\zeta$ .  $\epsilon_c$  and  $C$  are arbitrary constants taken as 0.15 and  $5.325 \times 10^4$  respectively for all the cases reported in this study. The sensitivity of global errors with a 10% variation in  $C$  are observed to be within 1%.

### 3. Numerical set-up

In this section, we discuss the transformed governing equations in curvilinear coordinates, spatial discretization, filtering schemes and the algorithms employed for the baseline code using upwind schemes and enhanced code using high-order explicit and compact schemes.

#### 3.1. Governing equations in general coordinates

The current solver is written in generalized (curvilinear) coordinate system with  $\xi$ ,  $\eta$ , and  $\zeta$  being the coordinate axis directions. Equations 2, 3 and 5 in Cartesian coordinates are transformed to curvilinear coordinates as given by the equations 8, 9 and 10 respectively. All the equations were non-dimensionalized with the reference length scale  $L_{ref}$  and time scale  $\tau$ .

**Eikonal equation:**

$$\hat{U} \frac{\partial \phi}{\partial \xi} + \hat{V} \frac{\partial \phi}{\partial \eta} + \hat{W} \frac{\partial \phi}{\partial \zeta} = 1 \quad (8)$$

**Hamilton-Jacobi equation:**

$$\hat{U} \frac{\partial \phi}{\partial \xi} + \hat{V} \frac{\partial \phi}{\partial \eta} + \hat{W} \frac{\partial \phi}{\partial \zeta} = 1 + \Gamma \left( \xi_x \frac{\partial U_x}{\partial \xi} + \eta_x \frac{\partial U_x}{\partial \eta} + \zeta_x \frac{\partial U_x}{\partial \zeta} + \xi_y \frac{\partial U_y}{\partial \xi} + \eta_y \frac{\partial U_y}{\partial \eta} + \zeta_y \frac{\partial U_y}{\partial \zeta} + \xi_z \frac{\partial U_z}{\partial \xi} + \eta_z \frac{\partial U_z}{\partial \eta} + \zeta_z \frac{\partial U_z}{\partial \zeta} \right) \quad (9)$$

Where,  $\hat{U}$ ,  $\hat{V}$  and  $\hat{W}$  are contravariant velocities and,  $U_x$ ,  $U_y$  and  $U_z$  are components of Eikonal front propagation velocity defined as follows:

$$\begin{aligned} \hat{U} &= \xi_x U_x + \xi_y U_y + \xi_z U_z \\ \hat{V} &= \eta_x U_x + \eta_y U_y + \eta_z U_z \\ \hat{W} &= \zeta_x U_x + \zeta_y U_y + \zeta_z U_z \\ U_x &= \frac{\partial \phi}{\partial x} = \xi_x \frac{\partial \phi}{\partial \xi} + \eta_x \frac{\partial \phi}{\partial \eta} + \zeta_x \frac{\partial \phi}{\partial \zeta} \\ U_y &= \frac{\partial \phi}{\partial y} = \xi_y \frac{\partial \phi}{\partial \xi} + \eta_y \frac{\partial \phi}{\partial \eta} + \zeta_y \frac{\partial \phi}{\partial \zeta} \end{aligned}$$

$$U_z = \frac{\partial\phi}{\partial z} = \xi_z \frac{\partial\phi}{\partial\xi} + \eta_z \frac{\partial\phi}{\partial\eta} + \zeta_z \frac{\partial\phi}{\partial\zeta}$$

**Poisson equation:**

$$\xi_x \frac{\partial U'_x}{\partial\xi} + \eta_x \frac{\partial U'_x}{\partial\eta} + \zeta_x \frac{\partial U'_x}{\partial\zeta} + \xi_y \frac{\partial U'_y}{\partial\xi} + \eta_y \frac{\partial U'_y}{\partial\eta} + \zeta_y \frac{\partial U'_y}{\partial\zeta} + \xi_z \frac{\partial U'_z}{\partial\xi} + \eta_z \frac{\partial U'_z}{\partial\eta} + \zeta_z \frac{\partial U'_z}{\partial\zeta} = -1 \quad (10)$$

where,

$$U'_x = \xi_x \frac{\partial\phi'}{\partial\xi} + \eta_x \frac{\partial\phi'}{\partial\eta} + \zeta_x \frac{\partial\phi'}{\partial\zeta}$$

$$U'_y = \xi_y \frac{\partial\phi'}{\partial\xi} + \eta_y \frac{\partial\phi'}{\partial\eta} + \zeta_y \frac{\partial\phi'}{\partial\zeta}$$

$$U'_z = \xi_z \frac{\partial\phi'}{\partial\xi} + \eta_z \frac{\partial\phi'}{\partial\eta} + \zeta_z \frac{\partial\phi'}{\partial\zeta}$$

### 3.2. Spatial discretization

#### 3.2.1. Baseline solver

Finite difference schemes are used for spatial discretization. The baseline solver employs first-order up-wind scheme to estimate advection analogous terms in the Eikonal and Hamilton-Jacobi equations; and  $2^{nd}$  order central difference scheme to estimate the Laplacian term in the H-J and Poisson equations. For example, the up-wind formulation used to estimate the first term of Eikonal equation (Eqn.8) on the LHS:  $\hat{U}\phi_x$ , is as shown below.

$$\hat{U}\phi_x = 0.5(\hat{U} + |\hat{U}|)B + 0.5(\hat{U} - |\hat{U}|)F \quad (11)$$

where,

$$B = \frac{\phi_i - \phi_{i-1}}{\Delta\xi_{i-1}} \quad \text{and} \quad F = \frac{\phi_{i+1} - \phi_i}{\Delta\xi_{i+1}} \quad (12)$$

'i' here corresponds to the index of grid points in the  $\xi$ -direction. The terms  $\frac{\partial\phi}{\partial\xi}$ ,  $\frac{\partial\phi}{\partial\eta}$  and  $\frac{\partial\phi}{\partial\zeta}$  which are required to compute  $\hat{U}$  are estimated as follows:

$$\frac{\partial\phi}{\partial\xi} \approx n_{i-1}F + n_{i+1}B \quad (13)$$

$$n_{i-1} = 0.25(1 + \text{SIGN}(1, F + B)) (1 + \text{SIGN}(1, B)) \quad (14)$$

$$n_{i+1} = 0.25(1 - \text{SIGN}(1, F + B)) (1 - \text{SIGN}(1, F)) \quad (15)$$

Similar upwind strategy, in the direction of the front propagation, is employed to estimate the metric terms and derivatives of  $\phi$  in other computational coordinate directions,  $\frac{\partial\phi}{\partial\eta}$  and  $\frac{\partial\phi}{\partial\zeta}$ .

### 3.2.2. Enhanced solver

In the enhanced solver, high-order spatial discretization schemes namely explicit second order (E2), explicit 4th order (E4), compact 4th order (C4) and compact 6th order (C6) schemes are used to discretize all the spatial derivative terms and metric terms present in the governing differential equations 8, 9 and 10. Implementation of these schemes was straight forward in the current work as most of the code components required were reused from the in-house high-fidelity fluid flow solver COMPSQUARE [17, 18, 19]. Following [7], the first-order derivative of a variable  $\phi$  in the interior domain is computed as:

$$\alpha\phi'_{i-1} + \phi'_i + \alpha\phi'_{i+1} = b\frac{\phi_{i+2} - \phi_{i-2}}{4\Delta\xi} + a\frac{\phi_{i+1} - \phi_{i-1}}{2\Delta\xi} \quad (16)$$

$\phi'$  represents derivative of  $\phi$  in  $\xi$  direction. While the constant  $\alpha$  is zero for explicit schemes (E2 and E4), it is non-zero for compact schemes (C4 and C6). Values of the coefficients 'a' and 'b' which vary with scheme along with the formulation of derivatives at the boundaries can be found in Ref.[7].

### 3.3. Solution convergence

Pseudo time iterations are used to drive the solution towards steady state. A pseudo time derivative ( $\frac{\partial\phi}{\partial t^*}$ ) has been added to LHS of all the three differential equations (Eqn.17 18 & 20) and marched explicitly in pseudo time ( $t^*$ ) with a four stage Runge-Kutta (RK) 4th order time integration. In addition, local-time stepping is used to accelerate the convergence.

$$\frac{\partial\phi}{\partial t^*} + \mathbf{U} \cdot \nabla\phi = 1 \quad (17)$$

$$\frac{\partial\phi}{\partial t^*} + \mathbf{U} \cdot \nabla\phi = 1 + (\nu\phi)\nabla^2\phi \quad (18)$$

$$\frac{\partial\phi}{\partial t^*} - 1 = \nabla^2\phi \quad (19)$$

Following convergence criterion is used to arrive at steady state solution:

$$\left| \frac{\phi - \phi_o}{L_{ref}} \right|_{max} \leq 10^{-8} \quad (20)$$

Here,  $\phi$  and  $\phi_o$  correspond to the wall distance values in the current and previous pseudo time iterations. The solution is converged until the maximum change in the wall distance value during a pseudo time step is below  $10^{-8}$  in the entire domain. For the unsteady cases, where the body(s) or the wall(s) move w.r.t time, the boundary conditions in the computational domain are updated at every physical time step and  $\phi$  is repeatedly computed. Between two physical time steps, pseudo iterations with local time-stepping are used to drive the solution to a steady state.

### 3.4. Filtering scheme

High frequency dispersion errors arising due to the non-dissipative nature of the high-order central schemes (E2,E4,C4 and C6), and the non-linear nature of the governing equations, can lead to convergence issues. To counter this, an implicit 10th order spatial filter proposed by Visbal et al. [7] is used to smoothen and hence stabilize the solution. The filtering order is reduced near the walls gradually up to second order. This spatial filter has been applied along all the directions, after each pseudo time step. Following [7], the implicit filtering operation of a variable  $\Phi$  along a direction  $i$  is given as:

$$\alpha_f \hat{\phi}_{i-1} + \hat{\phi}_i + \alpha_f \hat{\phi}_{i+1} = \sum_{n=0}^{n=N} \frac{a_n}{2} (\phi_{i+n} + \phi_{i-n}) \quad (21)$$

Where  $\phi$  and  $\hat{\phi}$  are unfiltered and filtered functional values respectively and  $\alpha_f$  is the filtering coefficient.  $2N$  is the order of filter which uses a  $2N + 1$  point stencil. A 10th order filter ( $N=5$ ) is used in the current work at interior points and  $\alpha_f$  in the current work varied between 0.46 and 0.495 for different test cases. Values of coefficients  $a_n$  for the 10th order filter and the low-order filters which were applied near boundaries are taken from [7].

### 3.5. Boundary Conditions and Initialization

Dirichlet boundary condition is imposed on the wall grid points, where the value of the wall distance is set to zero. Wall distance ( $\phi$ ) is also set to zero at all the grid points lying within the volume of the solid body/bodies.

$$\phi_{wall} = 0 \quad (22)$$

Neumann boundary condition, where the gradient of wall distance is set to zero, is imposed on the far-field boundaries.

$$\frac{\partial \phi}{\partial n} = 0 \quad (23)$$

Here,  $n$  is the direction normal to the boundary. The wall distance ( $\phi$ ) values are initialized to zero within the domain before starting the simulation. A flow chart describing the details the algorithm for the baseline and enhanced solver is shown in Figure 1.



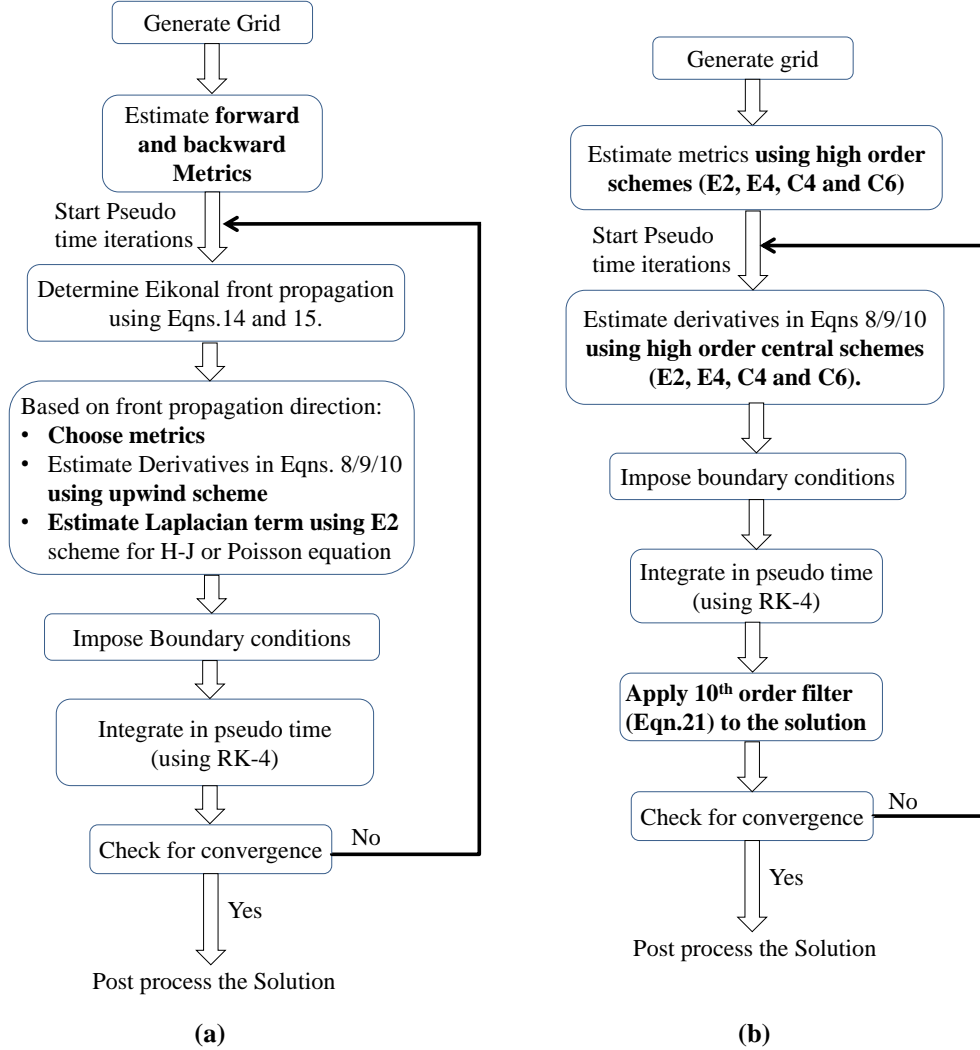


Figure 1: Algorithm flow chart for (a) Baseline UW solver and (b) Enhanced high-order solver

#### 4. Case set-ups and grid for validation

Both the steady and unsteady computation of wall-distances have been incorporated into the solver. The implementation has been tested and validated using eight canonical test cases. Table-1 lists the geometry, mesh resolution and boundary conditions used for the simulations.

Cases 1 and 2 are used to validate the baseline solver. Case-2, chosen from [4], demonstrates the capability of the wall-distance solver when complex geometries are present within the computational domain. Cases 3, 4 and 5 are used to validate the enhanced solver and compare the results against the baseline solver. Case-6 is solved to examine the effect of curvature on the accuracy of wall distances computed using H-J approach. Results using standard H-J and standard H-J based on the curvature corrections introduced by Nakanashi [22] are compared. We also discuss the modifications to the Nakanashi's [22] approach, which have improved the accuracy further. Cases 7 and 8 respectively

Case No.	Case name	Geometry and boundary conditions	Grid	Additional details
1	3-D box	10×10×10 m <sup>3</sup> 3-D cube shaped enclosed space with all its faces as walls.	41×41×41	-
2	Complex geometry	10×10 2-D square domain with multiple geometric shapes engraved into it. The edge of each shape is treated as wall.	101×101	-
3	Flat plate	10×10 2-D square domain with its bottom edge treated as wall.	32 × 32, 64 × 64, 128 × 128 and 256 × 256	-
4	Parallel plates	10×10 2-D square domain with its top and bottom edges treated as walls.	32 × 32, 64 × 64, 128 × 128 and 256 × 256	-
5	2-D box	10×10 2-D square domain with all it's edges treated as walls.	32 × 32, 64 × 64, 128 × 128 and 256 × 256	-
6	2-D circular bump	2.4×3.6 sized 2-D domain with a circular bump on bottom surface treated as wall.	41×41	-
7	Piston cylinder arrangement	2-D piston executing simple harmonic motion along vertical direction, inside a 5×10 cylinder	41×131	The frequency and amplitude of oscillating piston are specified to be 1.5 $\pi$ Hz and 3 units respectively.
8	Bouncing cube	2-D cube of size 1×1 bouncing in the presence of gravity inside a domain of dimensions 10×10, whose top and bottom are treated as walls	64×64	Acceleration due to gravity was taken as 9.81 units. The cube loses 10% of its total momentum after each bounce from the bottom wall.

Table 1: Case set-up, boundary conditions and grid details for various test cases.

simulate a piston-cylinder arrangement and a cube bouncing between parallel walls. These test cases demonstrate the efficacy of the unsteady solver where the wall-distances between the surfaces vary with time. In addition, we have also simulated the wall distance evolution inside a solid rocket motor with a progressively burning star-grain shaped propellant. This test case is based on the simulations presented in [11].

## 5. Results

In this section the baseline solver which employs first order up-wind scheme is validated on cases 1 and 2 (3-D box and Complex geometries). Subsequently, the enhanced solver is validated on rest of the test cases. For all the test cases, we compare the wall-distance and the error field computed from enhanced solver against the exact results and those obtained using the baseline solver. The exact solution was found analytically based on the case geometry, as most of the test cases used in this work are canonical in nature. Computational time (CPU time) required by each of these methods are also compared.

### 5.1. Validation of the baseline solver

Figures 2(a,b,c) show the wall-distance field computed for case-1 on  $Z = 5$  plane. Solutions corresponding to Eikonal, H-J and Poisson equations are compared here. Corresponding errors w.r.t the exact wall-distance is compared in Figures 2(d,e,f). Figure 2(g) compares the wall-distance on a vertical line passing through the domain's geometric center. It is evident that, for all the approaches, the errors are negligible very close to the walls. However, the error increases with increasing distance from the wall particularly using the Poisson approach. On the other hand, the predictions of both the Eikonal and H-J are much more accurate, with the Eikonal solution being the most accurate throughout the domain. The loss of accuracy of the H-J approach away from the walls is attributed to the Laplacian term using the standard  $\Gamma$  formulation.

Figure 3 compares the computed wall distance contours for case-2 using all the three differential equations. The wall-distance field obtained is in agreement with the results reported in [4]. It also demonstrates the robustness and performance of the current solver in handling geometries with complex shapes. Having validated the baseline solver using the upwind schemes, we have attempted to solve the same set of differential equations with the higher order schemes inbuilt in the in house solver COMPSQUARE.

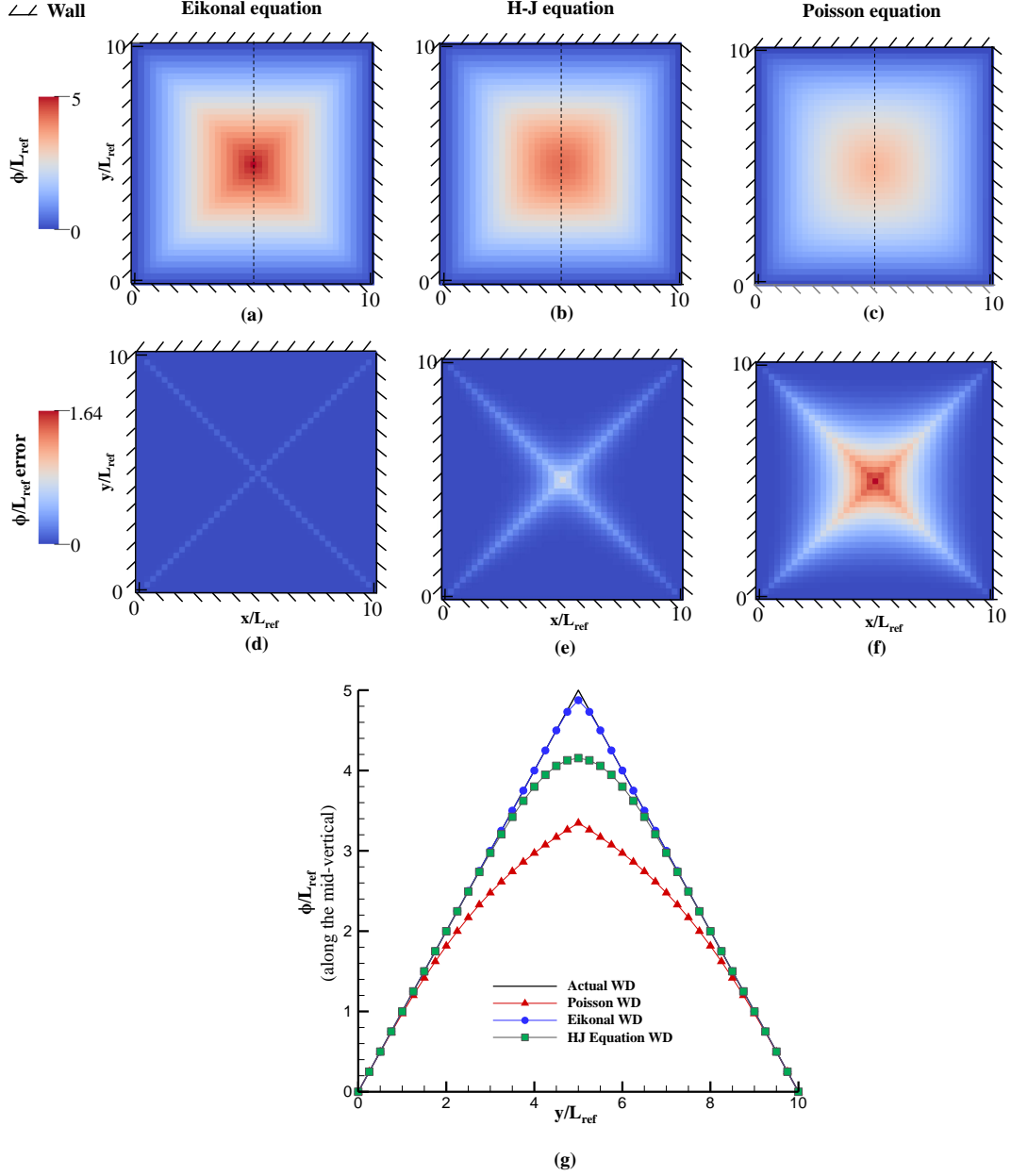


Figure 2: Wall distance field (a,b,c) and the corresponding error field (d,e,f) for 2-D box case (case-1) obtained by solving (a,d) Eikonal equation, (b,e) Hamilton-Jacobi equation and (c,f) Poisson equation with the baseline solver. Figure (g) Compares the wall distance values along the mid-vertical line (represented in first three images) obtained using Eikonal, H-J and Poisson equations with the exact solution.

### 5.2. Effect of high order schemes and LAD based formulation on H-J solution

As demonstrated in the flow chart of Figure 1(b), the wall-distance solver has been enhanced to use high order discretization and filtering schemes. A new LAD based formulation for  $\Gamma$  (Eqn. 7) in the H-J equation, as discussed

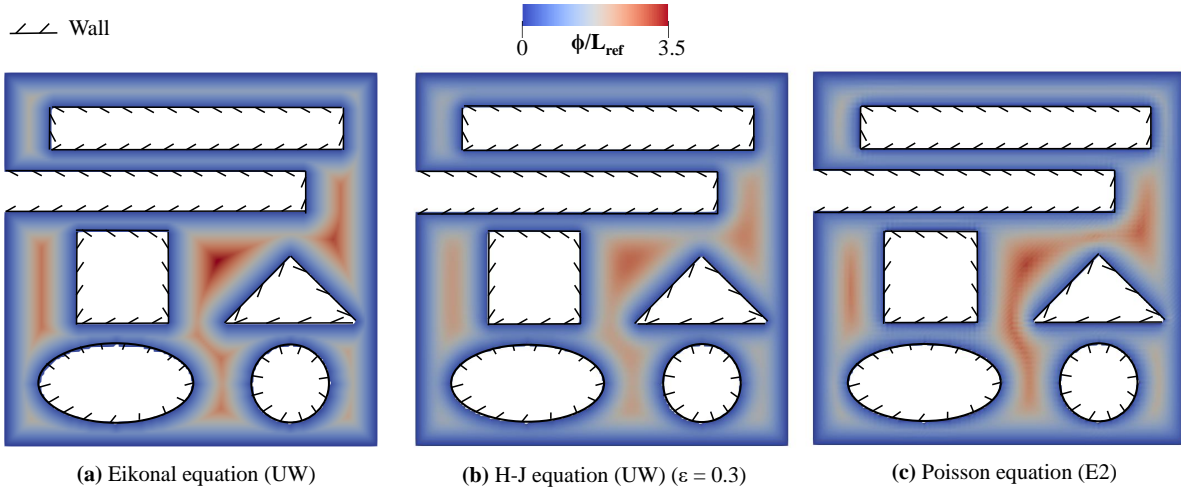


Figure 3: **Wall distance field obtained using (a) Eikonal, (b) Hamilton-Jacobi and (c) Poisson equations for complex geometries case (case-2).**

in section 2.3.2, has also been incorporated. Explicit 2nd order (E2), Explicit 4th order (E4), Compact 4th order (C4) and Compact 6th order (C6) spatial schemes with a 10th order filter are used instead of the first order UW scheme to enhance the solver in terms of both accuracy and speed.

Figures 4, 5 and 6 presents the contours of wall distance ( $\phi/L_{ref}$ ) and the corresponding errors for the canonical test cases of ‘Flat plate’, ‘channel’ and ‘2-D box’ respectively. The computational set-up and boundary conditions for these validation studies are described in Section 4. For clarity, we have also included line plots of the wall distance and errors along the vertical line (marked with dotted lines in the corresponding figures) for the baseline and enhanced solvers. From these set of results (Figs 4(g,h), 5(g,h) and 6(g,h)) the LAD based H-J formulation has been observed to yield the minimum error. The results are in close agreement with the exact solution for all the three validation test cases. This selective amount of dissipation added using the LAD formulation (Eqn.5 and 7) has improved the global accuracy while maintaining the stability. On the other hand, it is also apparent from these plots that the high order schemes (E2, E4, C4 and C6) show superior accuracy than the UW scheme. Even in the absence of LAD based formulation, the error at the near wall regions using high order schemes is lower than the UW scheme where the standard H-J formulation is designed to work.

The global  $L^1$  and  $L^2$  norms are quantified according to the integral p-norm defined as  $L^p = \left( \Delta x \Delta y \sum_i \sum_j |\phi - \phi_{exact}|^p \right)^{1/p}$ . Figure 7 compares these errors for the ‘parallel plates’ case at various grid resolutions. The global errors plotted in Fig.7, also support the argument that LAD based formulations and high order schemes work better than the baseline UW solver in terms of computing accurate wall distances. In addition to the improvements in the accuracy, the enhanced solver is also computationally economical. Figure 8 compares the computational time per 100 iterations for baseline and enhanced H-J solvers. All the simulations are carried out on a single processor (Dell Optiplex 3070 tower using 3 GHz Intel Core i7-9700 CPU with 32 GB/2666 MHz DDR4 memory). The explicit schemes (E2 and E4)

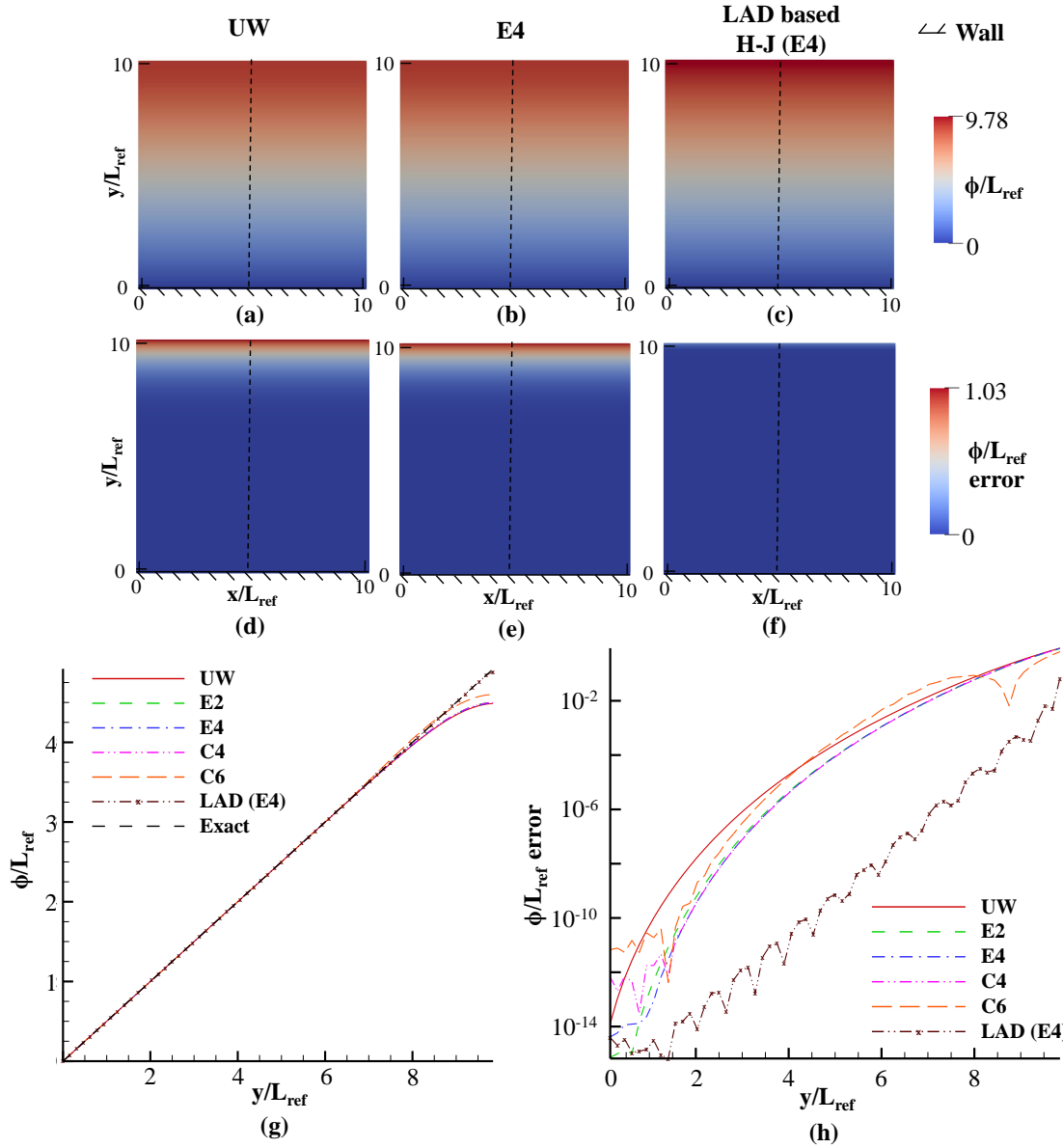


Figure 4: Wall distance field (a and b) and absolute wall distance error field contours (c and d) using UW, E4 and LAD based results for ‘flat plate’ case using H-J equation. Plots of wall distance (e) and absolute wall distance error (f) along mid vertical line (marked with dashed lines in images a-f) using various schemes. An  $\alpha_f$  of 0.48 was used for this case.

employing the standard and LAD based H-J formulation, are  $\approx 5-9$  times faster than the baseline solver. LAD based H-J formulation involves computing  $\Gamma$  during each iteration and are hence xx times slower than the standard H-J formulation using explicit schemes. Interestingly, the computational times required by the baseline solver using UW schemes and the enhanced solver using compact schemes to solve the LAD based H-J equation are almost similar. To summarize, the advantage of using high-order schemes (with filtering) over the UW schemes, both in terms of the

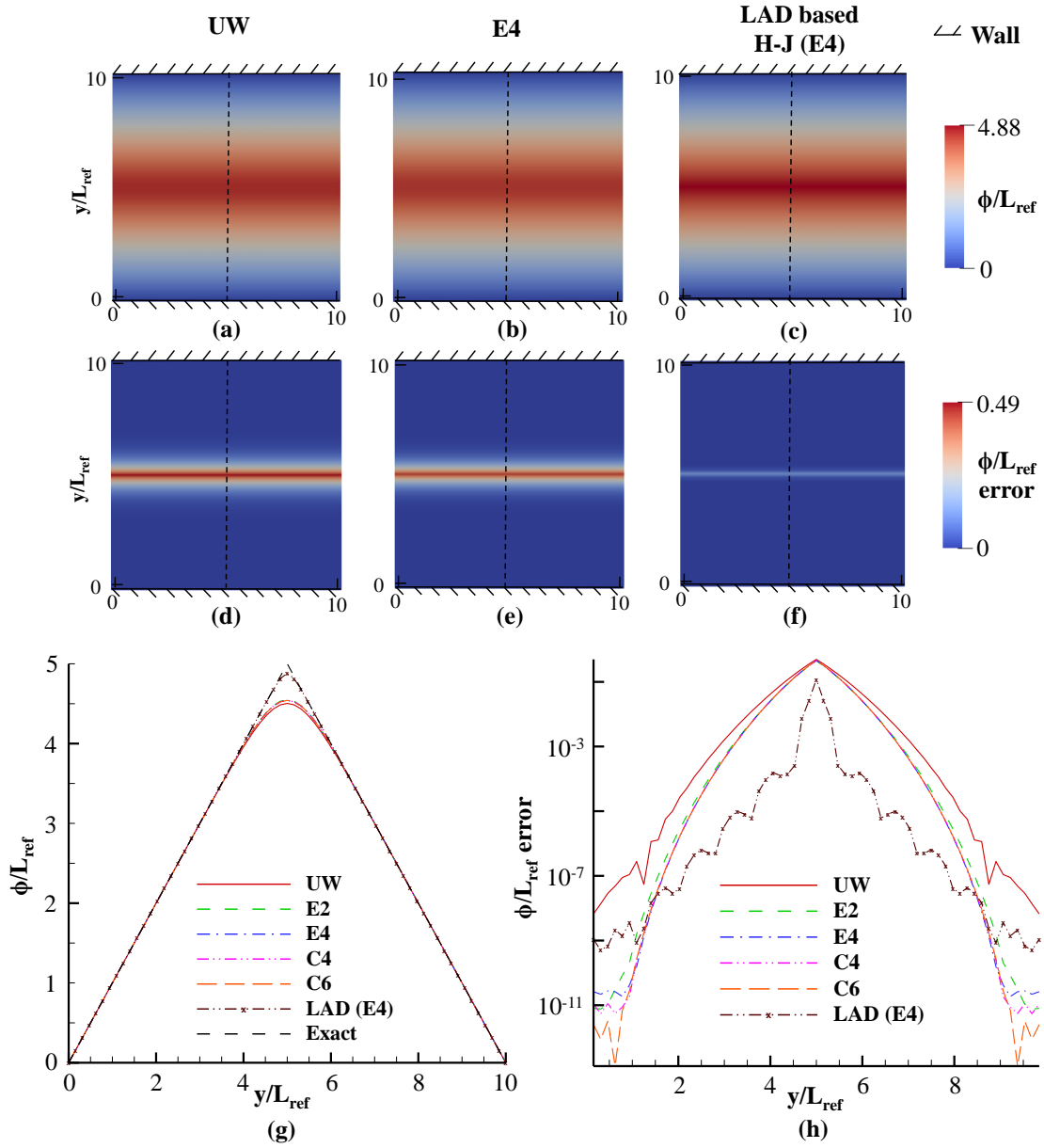


Figure 5: Wall distance field (a and b) and absolute wall distance error field contours (c and d) using UW, E4 and LAD based results for ‘channel’ case using H-J equation. Plots of wall distance (e) and absolute wall distance error (f) along mid vertical line (marked with dashed lines in images a-f) using various schemes. An  $\alpha_f$  of 0.48 was used for this case.

accuracy and computational time, can be clearly appreciated while solving the H-J equation.

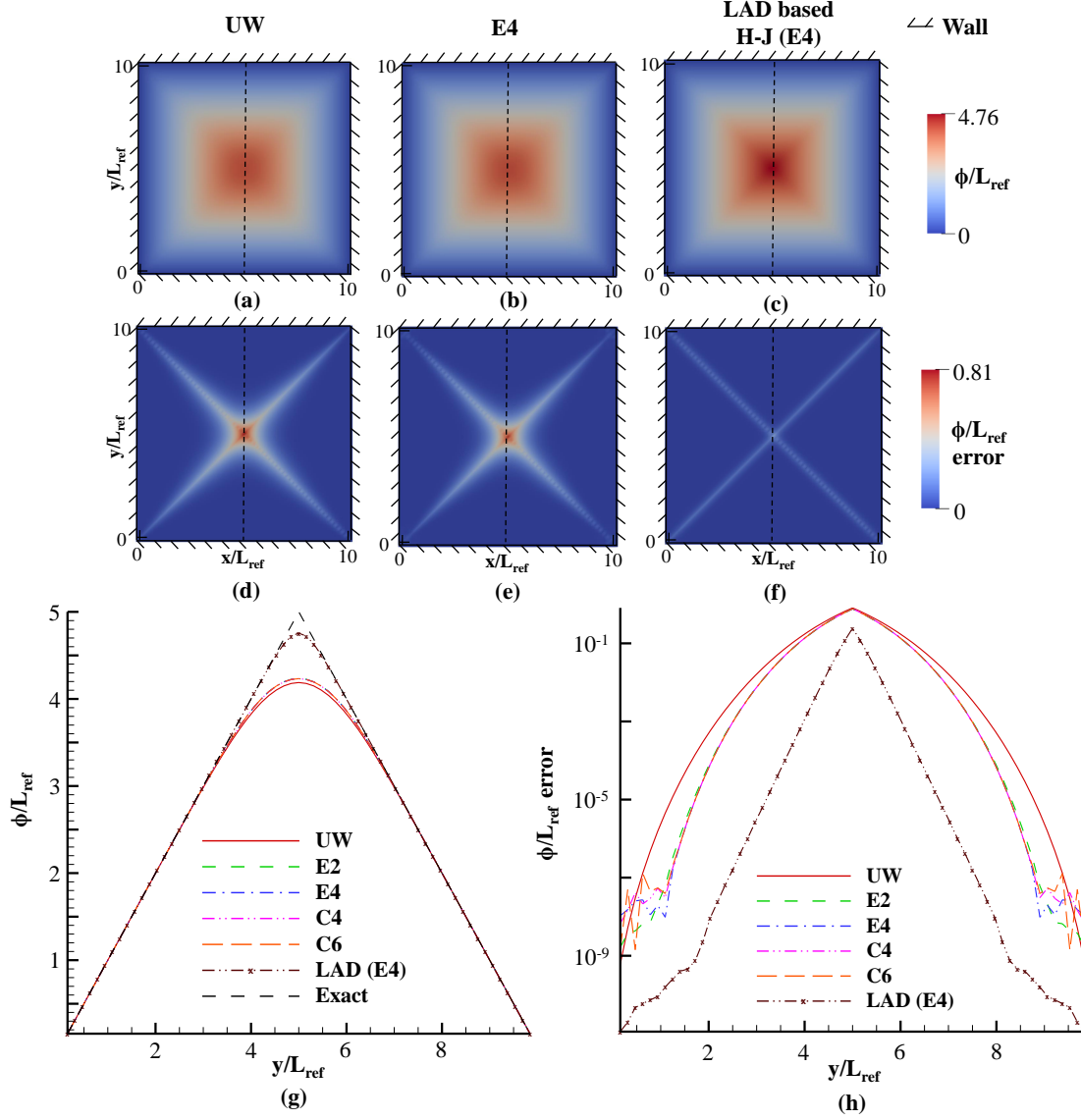


Figure 6: Wall distance field (a and b) and absolute wall distance error field contours (c and d) using UW, E4 and LAD based results for ‘2-D box’ case using H-J equation. Plots of wall distance (e) and absolute wall distance error (f) along mid vertical line (marked with dashed lines in images a-f) using various schemes. An  $\alpha_f$  of 0.46 was used for this case.

### 5.3. Effect of High order schemes on Eikonal equation solution

Inline with the analysis carried out in the previous section for the H-J equation, we have tested the computational advantage of using high-order schemes to solve the Eikonal equation. Performance of various schemes is tested on the ‘2-D box’ case. The wall distance and the error contours with corresponding plots along mid vertical line through the domain center are shown in the figure 9. The wall distance contours for the UW scheme and E4 scheme are largely identical (9(a,b)). The wall distance plots along the dashed lines marked in figure 9(e) are also in close



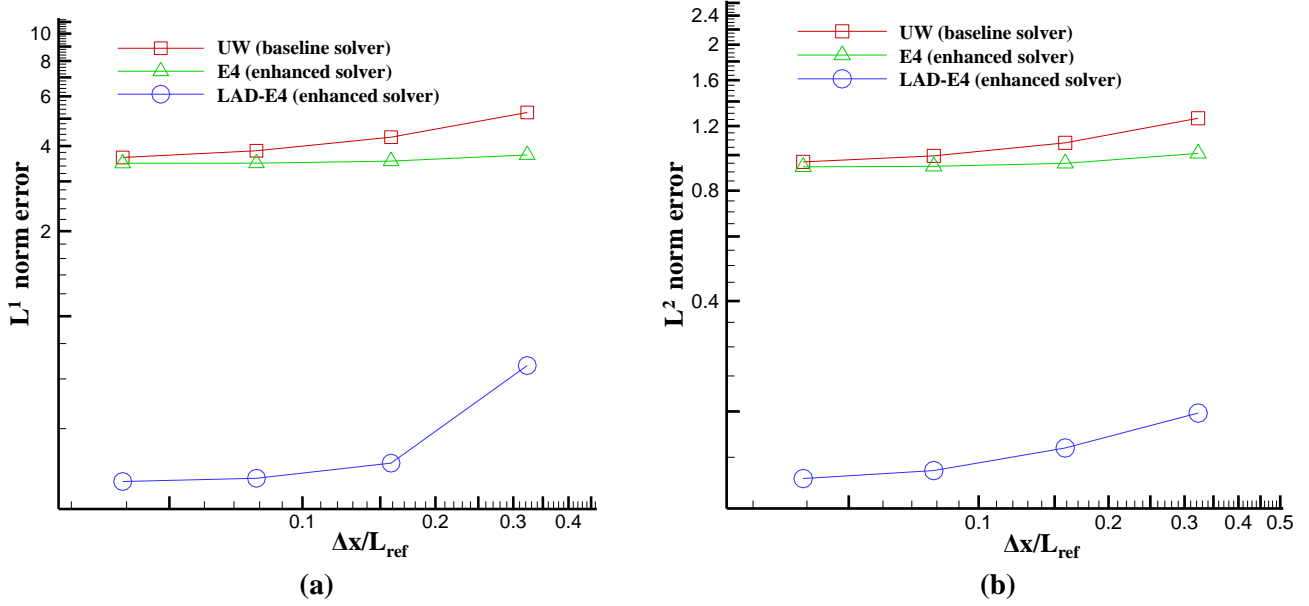


Figure 7:  $L^1$  and  $L^2$  norm errors for parallel plates case at various grid resolutions, using the UW scheme (baseline solver), E4 scheme and LAD approach.

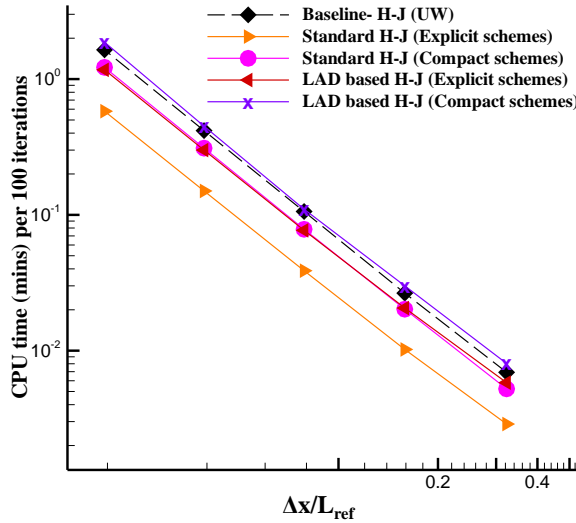


Figure 8: Comparison of CPU time taken per 100 iterations between baseline (UW scheme) and enhanced (corresponding to high-order schemes and LAD) solver tested using ‘2-D box case’.

agreement. However, when compared to the H-J equation, the Eikonal equation is hyperbolic and high-order schemes are susceptible to stability issues due to the lack of the Laplacian term. Table 2 lists out the  $L^1$ ,  $L^2$  and  $L^\infty$  norm errors corresponding to the baseline (UW) and enhanced solver (high order schemes) for all the three validation cases. It is evident from the table that the errors for the first two cases (‘flat plate’ and ‘channel’) using UW scheme are much lower ( $10^{-5}$ ) than the errors the high-order schemes ( $10^{-2}$ ). However, for the ‘2-D box’ case the errors

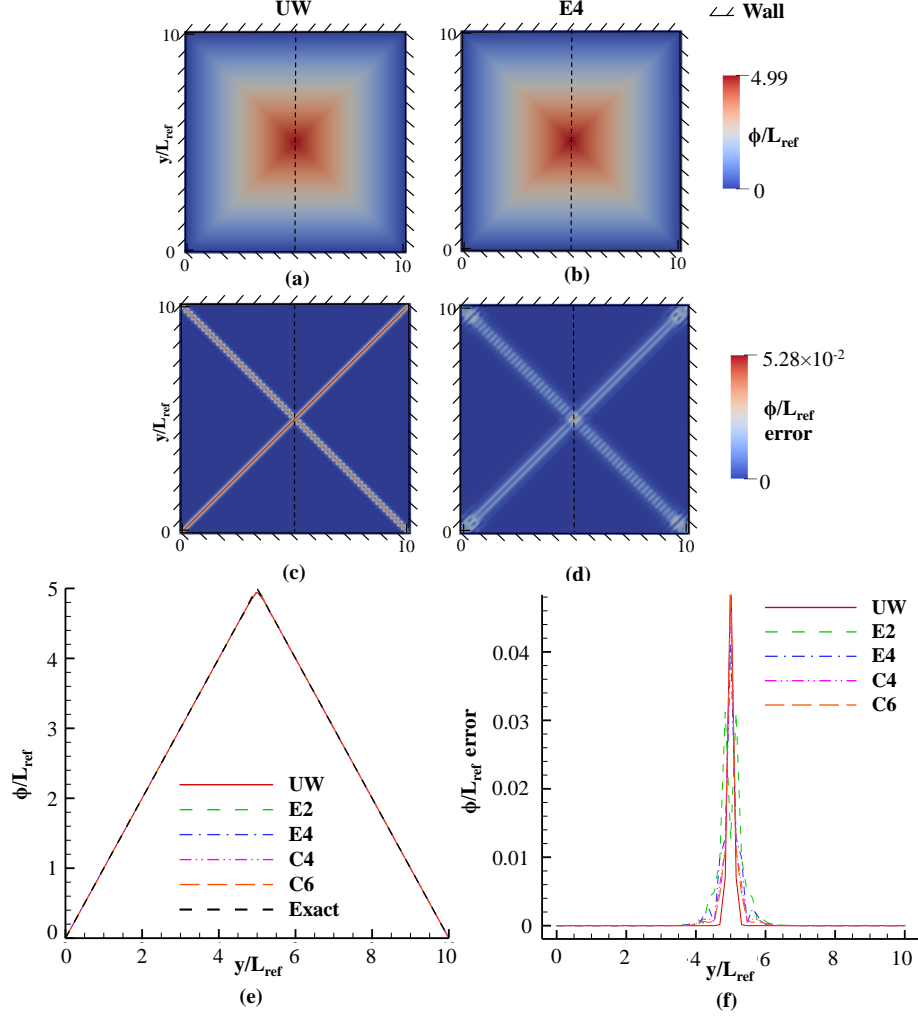


Figure 9: Wall distance field (a and b) and absolute wall distance error field contours (c and d) contours using UW and E4 schemes for ‘2-D box’ case using Eikonal equation. Plots of wall distance (e) and absolute wall distance error (f) along mid vertical line (marked with dashed lines in images a-f) using various schemes. An  $\alpha_f$  of 0.46 was used for this case.

	Case: Flat plate			Case: Parallel plates			Case: 2D Box		
	$L^1$	$L^2$	$L^\infty$	$L^1$	$L^2$	$L^\infty$	$L^1$	$L^2$	$L^\infty$
<b>UW</b>	1.75E-05	1.13E-05	8.76E-06	2.32E-05	1.80E-05	1.95E-05	5.14E-02	3.33E-02	2.64E-02
<b>E2</b>	2.11E-01	7.81E-02	5.12E-02	4.56E-02	2.17E-02	1.57E-02	4.67E-02	1.61E-02	1.58E-02
<b>E4</b>	6.56E-02	1.97E-02	1.04E-02	3.71E-02	2.01E-02	1.94E-02	3.77E-02	1.45E-02	1.91E-02
<b>C4</b>	8.10E-02	2.53E-02	1.25E-02	3.41E-02	2.14E-02	2.23E-02	3.41E-02	1.50E-02	2.21E-02
<b>C6</b>	5.66E-02	1.89E-02	8.33E-03	3.28E-02	2.20E-02	2.33E-02	3.30E-02	1.54E-02	2.31E-02

Table 2:  $L^1$ ,  $L^2$  and  $L^\infty$  norm errors for flat plate, parallel plates and 2-D box cases (under a grid resolution of  $128 \times 128$ ) using baseline solver (UW scheme, shaded row) and enhanced solver.

corresponding to baseline and enhanced solver are comparable. It implies that although the dispersion errors due to Gibbs phenomenon are partially suppressed due to the filtering, thereby enhancing the stability, the errors due to high-order schemes are larger when compared to the upwind scheme. Nevertheless, the maximum value of errors are still within the order of  $10^{-2}$  for all the three cases simulated.

Figure 10 compares the computational time required for 100 pseudo iterations for the baseline and enhanced Eikonal solvers, for ‘2-D box’ case at various grid resolutions. Due to the lack of the Laplacian term, the computational cost associated with solving Eikonal equation is relatively lower than H-J. On the other hand, the trends are similar to those observed in Fig.8. Explicit schemes (E2 and E4) and compact schemes (C4 and C6) are  $\approx 9$  to 10 times faster than the baseline solver. To summarize, while solving Eikonal equation, high order schemes with filtering are faster than the UW schemes. However, the global accuracy of these schemes is affected by the Gibbs phenomena.

From the sections 5.2 and 5.3, we choose explicit 4th order approach (E4) for solving H-J with LAD scheme and Eikonal equations to compute the wall distances. The judgement is based on both the accuracy and the computational benefit obtained using this approach. In the subsequent sections, we employ this approach to address the simulations on unsteady problems where the wall-distance varies with time.

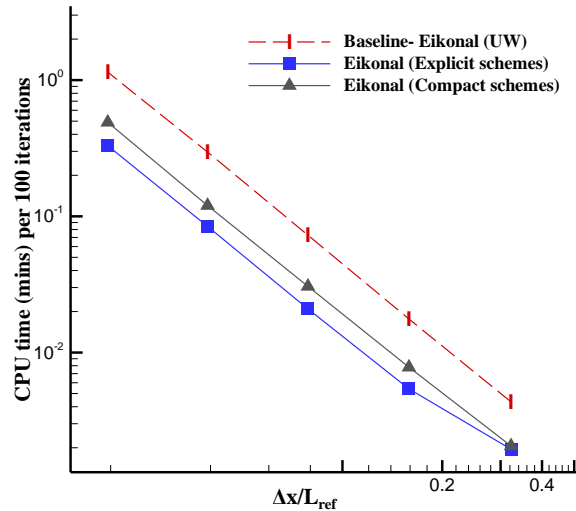


Figure 10: Comparison of CPU time taken per 100 iterations between baseline (UW scheme) and enhanced solver (which employs high-order explicit and compact schemes), tested using ‘2-D box case’.

#### 5.4. Effect of wall curvature and Nakanishi's modification

The Laplacian term in H-J equation is dependent on the wall curvature and can assume very high or low values near convex and concave regions of the domain respectively. As a result, the H-J equation largely deviates from the Eikonal equation which results in high wall distance errors. Mathematically,  $|\nabla^2\phi| \gg 0$  for convex regions. Hence, the RHS of the H-J equation  $|\nabla\phi| = \sqrt{1 + \Gamma\nabla^2\phi}$  will be much more greater than 1 in highly curved regions, there by significantly deviating from the Eikonal equation. For example, this effect can be seen at the airfoil leading and trailing edges. To counter this, Nakanishi [22] has proposed modifications to the original H-J equation. A curvature ( $\kappa$ ) based correction is introduced into the formulation which can eliminate the influence of convex wall curvature on wall distance solution. The modified form reads as follows.

$$\mathbf{U} \cdot \nabla\phi = 1 + (\epsilon\phi + \nu) \{ \nabla^2\phi - \text{MAX}(0, |\nabla\phi|\kappa) \} \quad (24)$$

The expressions for  $\nu$  (which is introduced to enhance stability) and  $\kappa$  are as follows:

$$\begin{aligned} \nu &= 0.001(1 - |\nabla\phi|)^2 \\ \kappa &= \nabla \cdot \mathbf{n}, \mathbf{n} = \frac{\nabla\phi}{|\nabla\phi| + \epsilon_0} \end{aligned}$$

In the absence of filtering, the simulations with this formulation using E2 and E4 schemes are observed to be unstable due to large dispersion errors. To counter this, the value of  $\epsilon$  can be increased, say to 1, as proposed by Nakanishi [22]. However, higher values of  $\epsilon$  (a) reduce the wall distance accuracy away from the walls and (b) reduce the stable pseudo time-step ( $\Delta t^*$ ) thereby increasing the simulation time. To account for these accuracy and convergence issues, we have reduced the value of  $\epsilon$  to 0.2 and used filtering (with  $\alpha_f = 0.495$ ). We refer this approach as 'Modified Nakanishi' in the plots.

The computational grid used for the simulations of 'circular bump' validation case is shown in Fig.11(a). Also shown in Figures 11 (b-d) are the wall distance and wall-distance absolute error fields for 'circular bump' case using the standard H-J and modified Nakanishi approaches. From the wall distance and error plots shown in figures 12 (a) and (b), the effect of Nakanishi's formulation in mitigating the wall distance error can be clearly appreciated. The wall distance deviates from the exact solution using standard H-J approach. On the other hand, the modified Nakanishi solution rectifies the curvature related issues and predicts accurate wall distances in most of the domain, particularly near the walls.

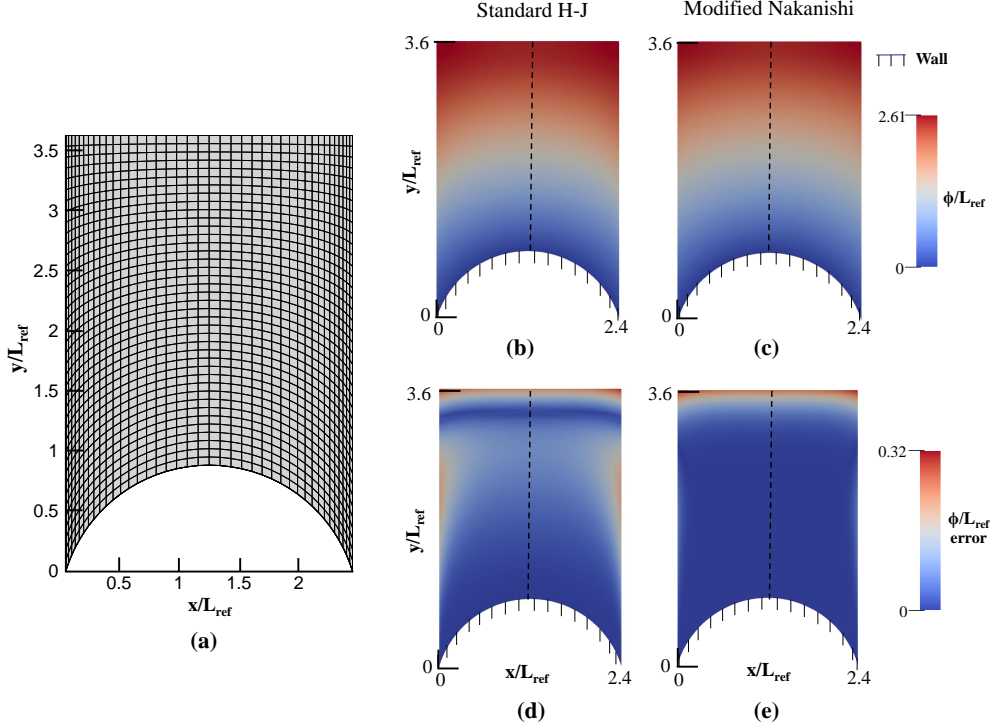


Figure 11: (a) The  $64 \times 64$  Computational grid used for the simulations; Comparison of Wall distance ( $\phi/L_{ref}$ ) and wall distance error contours ( $\phi/L_{ref}error$ ) between (b,d) standard H-J approach and (c,e) Modified Nakanishi approach. Both the simulations use E4 scheme with  $\alpha_f = 0.495$ .

### 5.5. Unsteady cases

In this section, we discuss the results from unsteady test cases to compute unsteady wall distances. The results obtained for the 2D test cases: ‘piston cylinder arrangement’ (case-7), ‘bouncing cube’ (case-8) and ‘star grain burnback in solid rocket motor’ using the Eikonal and H-J approach with E4 scheme are presented here. The computational set-up, grid and boundary conditions for these cases are described in Section 4.

Figures 13(a), 14(a), and 15 show the temporal variation of the H-J wall-distance field for the ‘piston-cylinder arrangement’, ‘bouncing cube’ and ‘star grain solid propellant burnback’ test cases respectively. The conventional method of computing wall distances using search methods are particularly expensive in these kind of scenarios where the walls are moving. It has been observed that the simulation time for the unsteady cases reduced drastically after the first physical time-step. The solution at the previous physical time step provides a close enough initial condition for the new physical time step. A probe, marked in Fig 13(a) and Fig 14(a), is placed in the domain to record the temporal variation of the wall-distance field. The corresponding temporal variation is compared against the exact solution in Fig 13(b) and Fig 14(b). The predictions corresponding to both Eikonal and H-J solutions are in good agreement with the analytical data. For the bouncing cube case, every time the cube bounces off from ground it gradually loses its energy by 20% until it finally settles down on the bottom surface. Figure 14(b) shows the effect of bouncing on the evolution of exact and computed wall distance recorded at the probe. The periodic raise and fall

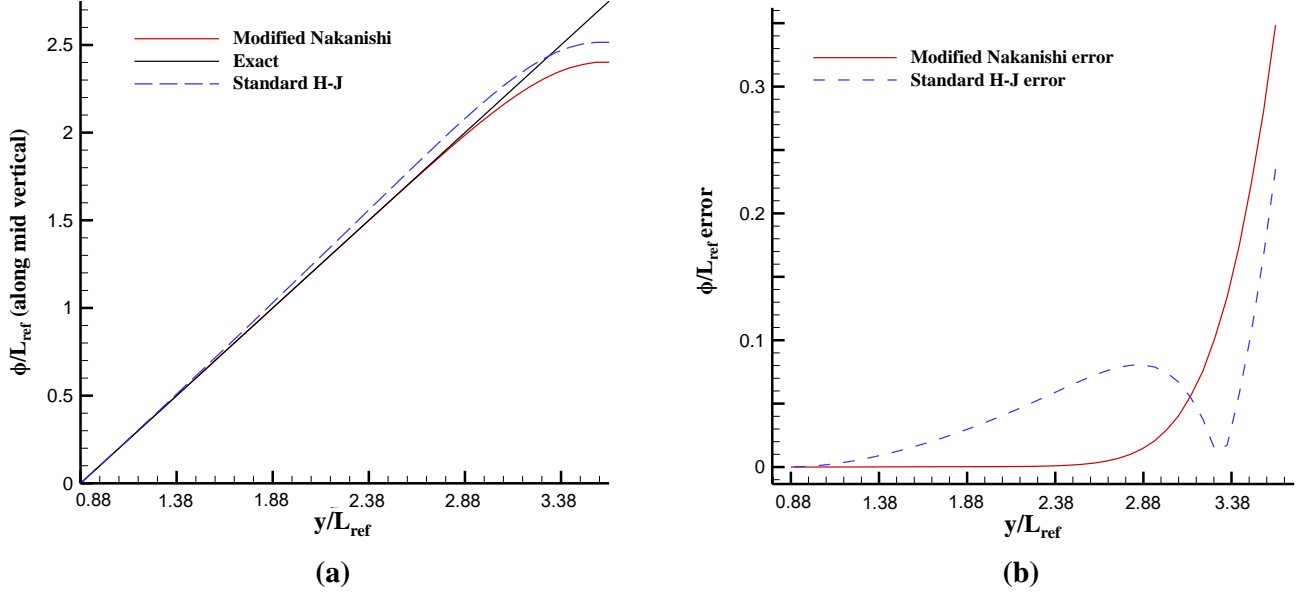


Figure 12: Comparison of (a) wall distance and (b) wall distance error obtained from the standard H-J and modified Nakanishi approach along the mid vertical of the computational domain.

events, with the asymptotic convergence of wall distance to a steady value with increasing time can be observed in the plot. Under the steady state, the probe is at a location which is farthest from all the walls. It has been demonstrated in Fig. 14 that standard H-J equation is less accurate away from the walls. Hence, the error between the analytical and predicted wall distance at  $t/\tau = 10-15$  is notable due to Laplacian operator in standard H-J equation. However, it is apparent from Figures 13(b) and 14(b) that the results using H-J with LAD scheme are much more accurate than the standard H-J and are in encouraging agreement with the Eikonal and exact solutions.

Wall distance evolution inside a solid rocket motor is also simulated. Figure 15 shows the unsteady burning of the propellant grain at different time instants. The evolution of the grain boundary is estimated using level-set approach. Subsequently, the coordinates of the grain boundary are fed to the unsteady wall-distance solver. It can be seen that, as the propellant burns inside the solid rocket motor (SRM), the grain boundary moves progressively away from the center. The sharp corners gradually smoothen out increasing the wall distance at the central portion as expected.

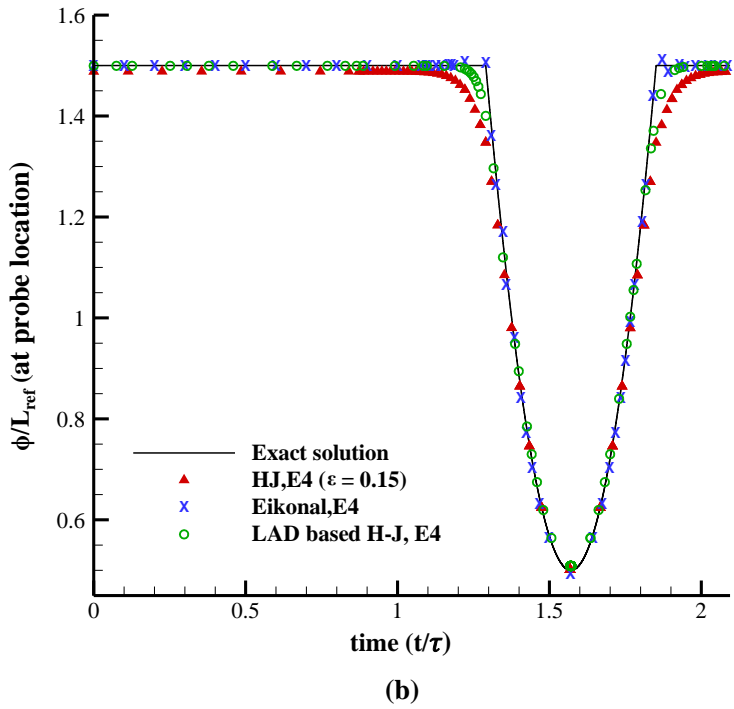
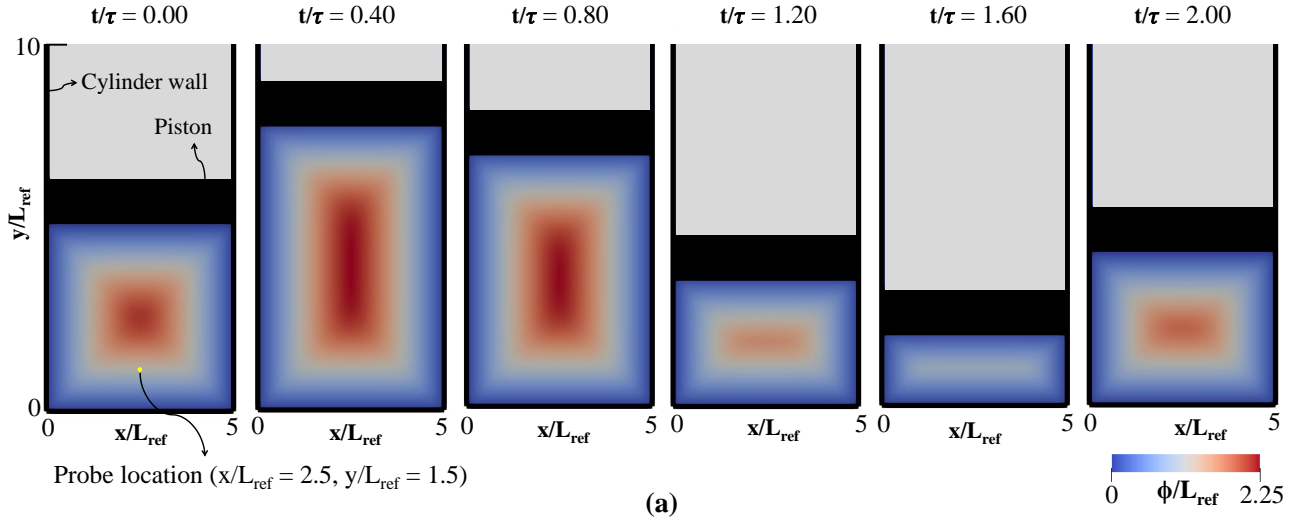
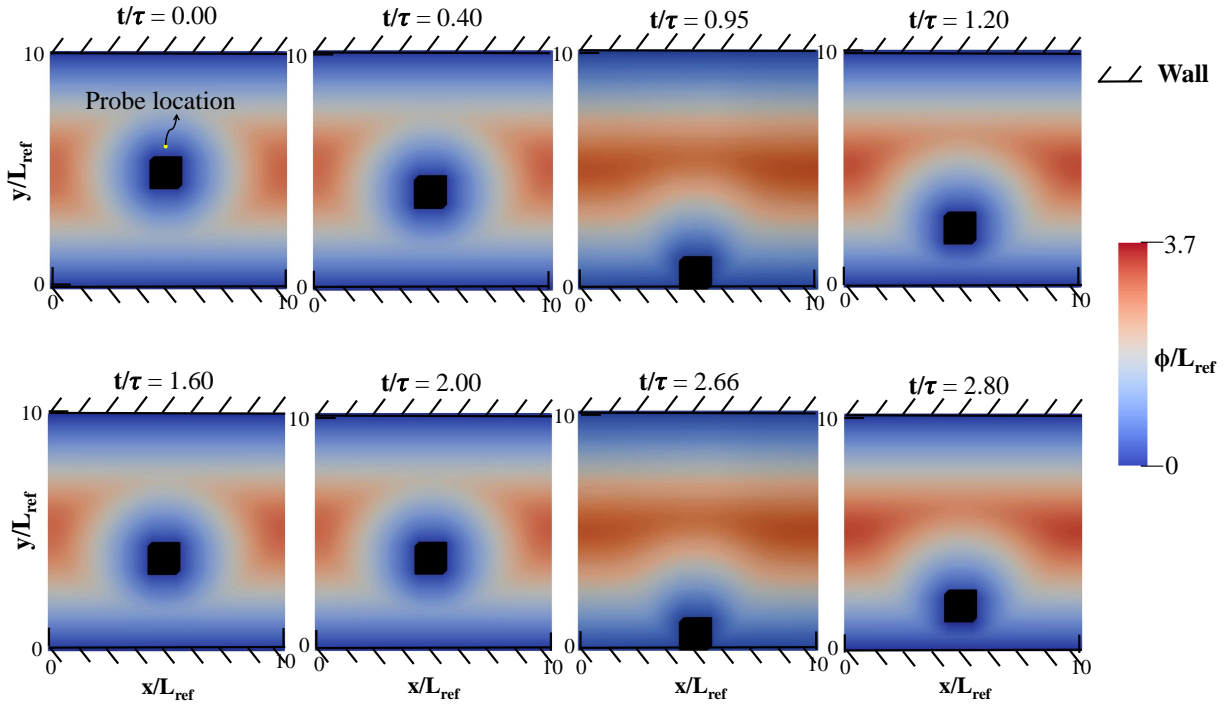


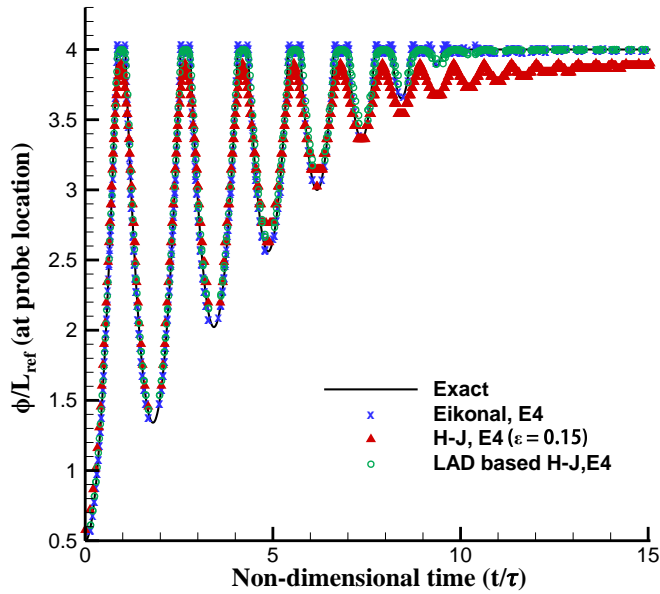
Figure 13: (a) Temporal evolution of wall distance field inside the piston-cylinder arrangement (case-\*) computed using H-J equation (with epsilon = 0.15) (b) Comparison of wall-distance evolution at the probe location shown in the first snapshot with the exact solution.

### 6. Conclusions

In this study, we have developed a computationally efficient differential equation based wall distance solver. Firstly, the baseline solver which employs the commonly used first-order upwind spatial discretization scheme is developed and validated on simple and complex geometries. The computational benefit of using high-order schemes (E2, E4,



(a)



(b)

Figure 14: (a) Temporal evolution of wall distance field around the bouncing cube (case-\*) computed using H-J equation (with epsilon = 0.15) (b) Comparison of wall-distance evolution with the exact solution at the probe location shown in the first snapshot.

C4 and C6) for wall-distance solvers, both in terms of accuracy and computational time, has been demonstrated. In addition, a modified Hamilton-Jacobi (H-J) formulation based on Localized Artificial Diffusivity (LAD) approach



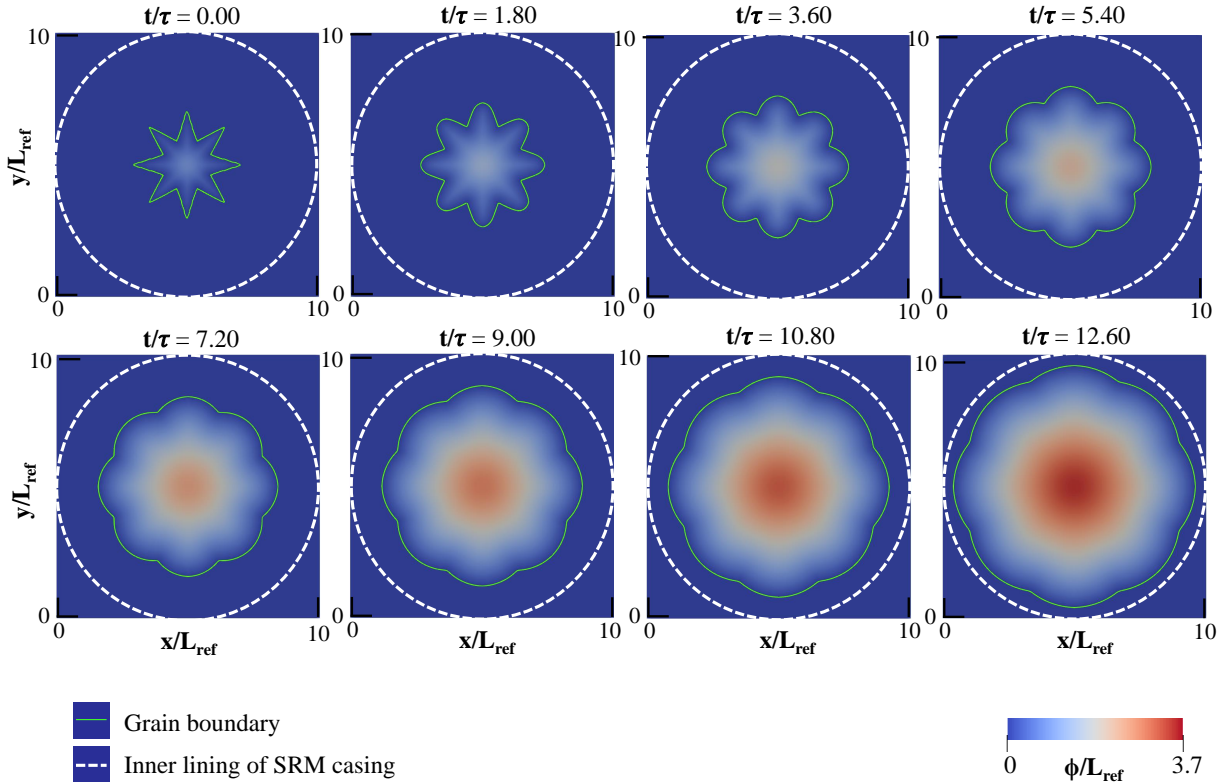


Figure 15: **Temporal evolution of wall distance field inside the combustion chamber of a solid rocket motor (with a 2-D eight legged star like propellant grain in it) computed using H-J equation.**

has also been proposed and validated. It is demonstrated to be much more accurate than the standard H-J approach using both the canonical test cases and also on the test cases where the wall-distance evolves with time. The unsteady test cases include ‘piston-cylinder arrangement’, ‘bouncing cube’ and wall-distance evolution inside the combustion chamber of a solid rocket motor due to the burning of a ‘star grain propellant’.

While solving the Hamilton-Jacobi equation, the high-order schemes performed approximately 5 – 9 times faster than the upwind schemes with a marginal improvement in the solution accuracy. The H-J based on LAD scheme produced results which are of comparable accuracy to the Eikonal solution. It’s solution accuracy is almost one order higher and the calculations are  $\approx 5$  times faster than the baseline H-J solver using upwind schemes. On the other hand, while solving the nonlinear hyperbolic Eikonal equation, the global error from high-order schemes is found to be larger when compared to the upwind schemes. Due to the lack of Laplacian operator in Eikonal equation, the central schemes suffered with some dispersion errors despite filtering. A modified curvature correction has been implemented in to the H-J solver to account for the error due to concave/convex wall curvatures.

## References

- [1] Tucker, P. G., Rumsey, C. L., Spalart, P. R., Bartels, R. E., and Biedron, R. T., *Differential equation-based wall distance computation for DES and RANS*, Journal of computational physics. Volume 190, Issue 1, 229-248 (2003)
- [2] Tucker, P. G., Rumsey, C. L., Spalart, P. R., Bartels, R. E., and Biedron, R. T., *Computations of wall distances based on differential equations*, AIAA journal, 43(3), 539-549. (2005)
- [3] Richard J. Jefferson-Loveday, V. Nagabhushana Rao, James C. Tyacke and Paul G. Tucker, *High-order detached eddy simulation, zonal LES and URANS of cavity and labyrinth seal flows*, Int. J. Numer. Meth. Fluids. (2013)
- [4] Tucker, P. G., *Hybrid Hamilton–Jacobi–Poisson wall distance function model*, Computers & fluids, 44(1), 130-142. (2011)
- [5] Jing-lei XU, Chao YAN, Jing-jing FAN. *Computations of wall distances by solving a transport equation*, Appl. Math. Mech. -Engl. Ed., 32(2), 141–150. (2011)
- [6] Anthony Bouchard, *Wall distance evaluation via Eikonal solver for RANS application*, Masters Thesis, UNIVERSITÉ DE MONTRÉAL. (2017)
- [7] Miguel R. Visbal and Datta V. Gaitonde, *High-Order Schemes for Navier-Stokes Equations: Algorithm and Implementation Into FDL3DI*, AFRL. (1998)
- [8] Jefferson-Loveday, R. J., Tucker, P. G., Northall, J. D., Nagabhushana Rao, V. *Differential equation specification of integral turbulence length scales*, Journal of turbomachinery, 135(3). (2013)
- [9] E. Fares W. Schröder, *A differential equation for approximate wall distance*, Int. J. Numer. Meth. Fluids, Volume 39, Issue 8, (2002)
- [10] Vadlamani, N. R., *Numerical investigation of separated flows in low pressure turbines*, Doctoral dissertation, University of Cambridge. (2014)
- [11] Arnau Pons Lorente, *Study of grain burnback and performance of solid rocket motors.*, Project report, Universitat Politècnica de Catalunya. (2013)
- [12] Spalart, P. R. and Allmaras, S. R. , *One-Equation Turbulence Model for Aerodynamic Flows*, La Recherche Aérospatiale, 1 (1994), pp. 5–21.
- [13] Sebastian G., Charbel F., *Fast computation of the wall distance in unsteady Eulerian fluid-structure computations*, Int. J. Numer. Meth. Fluids, Volume 89, Issue 4-5, 143-161 (2019)
- [14] Beatrice Roget, Jayanarayanan Sitaraman, *Wall distance search algorithm using voxelized marching spheres*, J. Comp Physics, Volume 241, 15 May 2013, Pages 76-94 (2013)

- [15] Les A. Piegl, Wayne Tiller, *Algorithm for finding all k nearest neighbors*, Journal of Computer Aided Design, Volume 34, Issue 2, 82-172 (2002)
- [16] Andrea Milli, Shahrokh Shahpar, *PADRAM: Parametric Design and Rapid Meshing System for Complex Turbomachinery Configurations*, ASME Turbo Expo, Copenhagen, Denmark (2012)
- [17] Achu, Shankar, and Nagabhushana Rao Vadlamani, *Entropically Damped Artificial Compressibility Solver Using Higher Order Finite Difference Schemes on Curvilinear and Deforming Meshes*. In AIAA Scitech 2021 Forum, p. 0634. (2021)
- [18] Vadlamani, Nagabhushana Rao, Paul G. Tucker, and Paul Durbin, *Distributed roughness effects on transitional and turbulent boundary layers*, Flow, Turbulence and Combustion 100, no. 3 p. 627-649. (2018)
- [19] Lin, Y., Vadlamani, R., Savill, M. and Tucker, P., *Wall-resolved large eddy simulation for aeroengine aeroacoustic investigation*, The Aeronautical Journal, 121 (1242), pp.1032-1050. (2017)
- [20] S. Kawai, S.K. Lele, *Localized artificial diffusivity scheme for discontinuity capturing on curvilinear meshes*, Journal of Computational Physics 227 (2008) 9498–9526
- [21] Spalding DB. Calculation of turbulent heat transfer in cluttered spaces. Presented at the 10th international heat transfer conference, Brighton, UK; (1994).
- [22] Tameo Nakanishi, *A Modification on Hamilton-Jacobi (HJ) Equation for Computing Wall Distances*, Trans. Japan Soc. Aero. Space Sci., Vol. 49, No. 163, pp. 55–57, (2006)